RSC Advances

PAPER

View Article Online
View Journal | View Issue

Cite this: *RSC Adv.*, 2023, **13**, 19803

Synthesis by adding CTAB and characterization of Ag@CuO@rGO nanocomposite with a novel core–shell crystal sugar structure and its application in supercapacitors

Yuxin Zhang,[a] Yong Li,*[a] Pengchong Yin [a] and Weizhong Han[ab]

In this study, we successfully synthesized Ag@CuO@rGO (rGO wrapped around Ag/CuO) nanocomposites using $AgNO_3$, $Cu(NO)_{32}$, and NaOH as raw materials and particularly treated CTAB as a template by chemical precipitation, hydrothermal synthesis, and subsequent high-temperature calcination processes. In addition, transmission electron microscopy (TEM) images revealed that the prepared products appeared to have a mixed structure. The results indicated that the best choice was CuO wrapped around Ag nanoparticles to form a core–shell crystal structure, and the crystal particles were arranged similarly to form an icing sugar block structure and were tightly wrapped by rGO. Moreover, the electrochemical test results demonstrated that Ag@CuO@rGO composite electrode material exhibited high pseudocapacitance performance; the material had a high specific capacity of 1453 F g^{-1} at a current density of 2.5 mA cm^{-2}, and the charging and discharging cycles remained constant up to 2000 times, indicating that the introduction of Ag improved the cycling stability and reversibility of the CuO@rGO electrode material and increased its specific capacitance, leading to the increase in the specific capacitance of supercapacitors. Therefore, the above results strongly support the application of Ag@CuO@rGO in optotronic devices.

Received 6th May 2023
Accepted 7th June 2023

DOI: 10.1039/d3ra03025c

rsc.li/rsc-advances

1 Introduction

The capacitive performance of supercapacitors depends on the selection of electrode materials.[1,2] Although the focus is on transition metal oxides, such as NiO, Co_3O_4, and Fe_2O_3,[3–5] their practical applications are limited owing to their high cost, high toxicity, and low catalytic activity. Further, it is particularly important to investigate a low-cost electrode material with high electrochemical activity and a large specific surface area.

Compared to other metal oxides, copper oxide belongs to a p-type transition metal oxide with a low band gap energy of only 1.2 eV.[6] Additionally, copper oxide has the advantages of low cost, easy preparation, excellent electrochemical activity, large

[a]School of Materials Science and Engineering, North China University of Water Resources and Electric Power, Zhengzhou 450045, China. E-mail: lionghuashui2020@gmail.com

[b]School of Materials Science and Engineering, Xi'an Jiaotong University, Xi'an 710049, China

Yuxin Zhang (PhD, Lecturer) is engaged in the controllable preparation of polymetallic modified electrode materials and the detection of their electrochemical properties and has published more than 8 SCI papers.

Yong Li (PhD, Associate Professor) is a reviewer of Analytical Methods, Journal of Non-Crystalline Solids, China Foundry and other journals.

specific surface area, and the ability to promote electron transfer at low overpotential, which makes it an ideal raw material for super electric electrodes.[7,8] However, copper oxide has comparatively low self-conductivity and is highly susceptible to agglomeration of nanoparticles during the preparation process, which can seriously affect the capacitance performance of the dielectric material.

The most effective way to solve the deficiency is to modify the surface of bare copper oxide materials, which can improve the capacitive property of supercapacitors by combining noble metal monomers, metal oxides, or carbon materials. It was found that they can forcefully connect with each other and manifest new functions in the nanocomposite system composed of copper oxide and noble metals, as a result of the difference in their properties, which in turn breaks the limitation of the single component of copper oxide.[9] Among them, silver (Ag) has electrophilic, nucleophilic, and special selectivity for the reaction, and is also the noble metal with the best electrical conductivity and low cost, so it is considered an intensely ideal doping material.[10,11] Another way is the combination of copper oxide and conductive carrier carbon material-graphene loaded together to synthesize a composite with a special structure. Namely, graphene has excellent physical and chemical properties, such as excellent mechanical properties, extremely stable load-bearing capacity, great specific surface area, and strong electron transport capacity;[12,13] there is especially no energy band gap but rather outstanding biocompatibility.[14]

Further studies demonstrated that the combination of CuO and rGO could exhibit better multiplicative performance, superior charging and discharging efficiency, and more stable cycling.[15] Therefore, rGO was used as the conductive carrier, and CuO was doped and modified with the advantage of nano-Ag to study the electrochemical properties of the electrode constructed by the three substances.[16–18] The experiments were carried out by chemical precipitation-hydrothermal synthesis and subsequent high-temperature calcination processes to synthesize Ag@CuO@rGO with the ternary nanostructure. Eventually, structural and electrochemical characterization was carried out, details involved the effects of different molar ratios of Cu and Ag and the surfactant on the morphology, also including the influence on the specific capacitance.

2 Experiments

2.1 Materials and methods

Graphene was purchased from Shenzhen Yuechuang Technology Co., Ltd, and cupric acetate ($Cu(Ac)_2$), DMF (AR, 99.5%), ammonium hydroxide ($NH_3 \cdot H_2O$, 25–28%), acetone, hydrochloric acid (HCL, 36–38%) and cetyltrimethylammonium bromide (CTAB) were obtained from Sinopharm Chemical Reagent Co., Ltd. Flexible conductive carbon cloth was purchased from Shanghai Hesen Electric Co., Ltd (SCRC, China). Potassium hydroxide (KOH), sodium hydroxide (NaOH), PVA, and anhydrous ethanol (C_2H_6O) were purchased from Macklin. Acetylene black and activated carbon (AC) were purchased from Cabot Corporation, USA. The chemical reagents were all analytical grade (AR) and the deionized water was prepared by a laboratory water purification system.

All reagents were analytically pure, including graphene, copper nitrate trihydrate, silver nitrate, CTAB, sodium hydroxide, potassium hydroxide, anhydrous ethanol, and deionized water (lab-made). In this work, a three-electrode system was used for the electrochemical experiments, *i.e.*, platinum sheet electrode, saturated glycerol electrode, and nickel foam coated with electrode material as the reference electrode, auxiliary electrode, and working electrode, respectively, connected with alligator clips and fixed in a 50 mL beaker, then to select the electrochemical test technique, and set the parameters.

First of all, a working electrode was prepared before the electrochemical experiment, next, 1 mol L^{-1} KOH of the alkaline electrolyte solution was added to the test mixture and activated at a sweep rate of 10 mV s^{-1} at −1 to 1 V to determine the specific potential window. Afterwards, a cyclic voltammetric scan was performed on the nickel foam electrode to analyze the effect of the sweep rate on the entire medium. In the end, constant current charge and discharge tests were performed to obtain the capacitance at different sweep rates.

2.2 Synthesis of Ag@CuO@rGO

Certain weights of silver nitrate ($AgNO_3$) and copper nitrate trihydrate ($Cu(NO)_{32} \cdot 3H_2O$) were taken in different molar ratios (Cu : Ag = 1 : 1, 1 : 2, 1 : 3), and labeled as $I_{1\text{-Cu}}$, respectively, $I_{2\text{-}}$

Pengchong Yin, Masters, engaged in the development and research of electrochemical sensors and supercapacitor electrode materials and carried out the preparation of modified clicks and the detection of their electrochemical properties.

Weizhong Han (Professor and Doctoral Supervisor). He has published more than 30 high-level papers in PRL, Nano Lett., Adv. Mater., Acta Mater., etc.

$_{Cu}$, I $I_{3\text{-}Cu}$ and $I_{1\text{-}Ag}$, I $I_{2\text{-}Ag}$, I $I_{3\text{-}Ag}$. After weighing three sets of monolayer graphene of the same mass 0.1 g, labeled rG_1, rG_2, rG_3, the same operation to obtain three sets of cetyltrimethylammonium bromide (CTAB) of the same mass 0.2 g, labeled CT_1, CT_2, CT_3.

Next, the graphene weighed above was firstly placed in beakers (150 mL), and 20 mL of deionized water was added to it and placed in the ultrasonic apparatus at 50 °C. In step two, three different masses of $AgNO_3$ and $Cu(NO)_{32}\cdot 3H_2O$ were placed in a 50 mL beaker, and 10 mL of deionized water was added to each beaker and stirred for 5 min, then the two solutions were mixed and stirred for 5 min. In step three, the surfactant CTAB was slowly added to the above three groups of solutions. Thereby, mixed solutions at 40 °C in the fourth step, graphene dispersion was added to the third step drop by drop and stirred and sonicated for 2 h at room temperature. In step five, 6.0 g of NaOH was weighed in a 100 mL beaker and 50 mL of deionized water was added and stirred magnetically for 10 min. In the end, 10 mL of NaOH solution was added drop by drop to the fourth step. The NaOH solution was added drop by drop to the mixed solution in the fourth step and stirred magnetically for 1 h to complete the precipitation reaction.

The following procedure involved hydrothermal reaction and high-temperature calcination. Firstly, the three groups of mixed solutions were transferred to an autoclave set at 180 °C for 10 h. After the hydrothermal reaction, the product was washed repeatedly with anhydrous ethanol and deionized water and then dried in a vacuum drying oven at 80 °C for 24 h. Eventually, the dried precursors were placed in a tube furnace at a heating rate of 4 °C min^{-1} to 400 °C, and held for 4 h. That is, the final products were obtained from different molar ratios (Cu : Ag = 1 : 1, 1 : 2, 1 : 3) to label as rGO-I_1, rGO-I_2, and rGO-I_3, respectively. Simultaneously, in this experiment, parallel comparisons were also performed. Under the same conditions, the molar ratio of Cu : Ag = 1 : 1 was used as the reference, hence the sample without CTAB was labeled rGO-I_4, and the sample was labeled rGO-I_5 in the case of calcination at 500 °C.

2.3 Fabrication of working electrode

In order to prepare the working electrode using the coating method, the study took nickel foam as a fluid collector and then configured the electrode material. For the Cuo@rGo composite, acetylene black and polytetrafluoroethylene emulsion (PTFE) were mixed well in the weight ratio of 75 : 15 : 10 and made into a paste. Subsequently, it was evenly coated on nickel foam pretreated with acetone, hydrochloric acid, and deionized water, using an area of 10 mm^2. Subsequently, it was dried under a vacuum at 80 °C for 10 h. Finally, it was pressed into the electrodes at a pressure of 10 Mpa.

3 Results and discussion

3.1 Structural and morphology of Ag@CuO@rGO

X-ray diffraction was performed to analyze the structure and components of silver–copper oxide/graphene nanocomposites (rGO-I_1, rGO-I_2, rGO-I_3, rGO-I_4, and rGO-I_5) (Fig. 1), the diffraction peak positions of the samples were consistent, which indicated that the main substances of the composites are essentially the same with five different molar ratios, as well as different temperatures and with or without active agents.

The diffraction peaks at 2θ angles at 32.5, 35.4, 38.7, 48.7, 53.5, 58.3, 61.5, 66.4, 68.1, 72.4, and 75.2, were ascribed to CuO(110), (11−1), (111), (20−2), (020), (202), (11−3), (310), and (310), respectively. (310), (220), (311), and (22−2) of the peaks of the crystalline surface (JCPDS No. 48-1548). The 2θ located at 38.1, 44.2, 64.4, 77.3, and 82.3, corresponded to the characteristic peaks of the Ag crystal plane (111), (200), (220), (311), and (222), respectively (JCPDS No. 87-0597). Fig. 1a shows that the sample rGO-I_1 had a diffraction peak located at 2θ = 15.5°, which is attributed to the crystal plane-diffraction (002) of graphene oxide, indicating the successful introduction of oxygen-containing groups into the graphene structure. Compared to the other samples, the diffraction peak at 2θ = 15.5°, which indicated that a small amount of unoxidized graphene was still present in the compound.

The samples rGO-I_2 and rGO-I_3 showed a clear broad peak at 2θ = 23.5° (002), revealing a further reduction in graphene oxide.[19] Fig. 1b illustrates the peak at (002) the crystal plane peaks of the rGO-I_4 and rGO-I_5 of the reduced graphene oxide could not be observed, suggesting that the aggregation of graphene lamellae was effectively suppressed, while the graphite was completely exfoliated, resulting in damage to the regular stacking structure of graphite, whose characteristic diffraction peaks would be weakened or even disappeared.[20] However, relative to the samples rGO-I_4 and rGO-I_5, the samples rGO-I_1 showed an extremely intensive crystalline diffraction peak of CuO(110), which is due to the high crystal strength and large mass share of the Ag@CuO, so the graphene diffraction peak was compressed behind the background peak of the compound.[21] Finally, a test was carried out in a surfactant (CTAB) using a molar ratio of Cu : Ag = 1 : 1.

Fig. 2 shows the morphology and characteristics of Ag@CuO@rGO using TEM analysis. The rGO-I_1 samples of Ag@CuO were uniformly distributed on the inner side of the rGO layer, displayed in (Fig. 2a and c), its overall structure consisted of individual crystals stacked in an icing sugar block-like structure. Moreover, the RGO owns a typical carbon layer, if a transparent and wrinkled silk yarn was folded together, and coated on the inner side of Ag@CuO. In addition, the rGO-loaded Ag@CuO shows ideal crystallinity and a smooth surface, Fig. 2b. The particle size was about 100 nm, which is more rewarding for charge and ion transport, especially without clumping.

With the addition of silver nitrate, rGO-I_2 will generate a small amount of agglomeration, as shown in Fig. 2d–f. The images (Fig. 2g–i) revealed that rGO-I_3 had an irregular mixed structure (pea-like and icing sugar lump-like) by rGO encapsulated on the outside of Ag@CuO, and also addresses a small amount of the agglomerated state. The reason is the amount of an increase in silver nitrate, which leads to a gradual increase in the particle size of Ag@CuO, and the adsorption capacity between ions will exceed the optimal strength, this will make

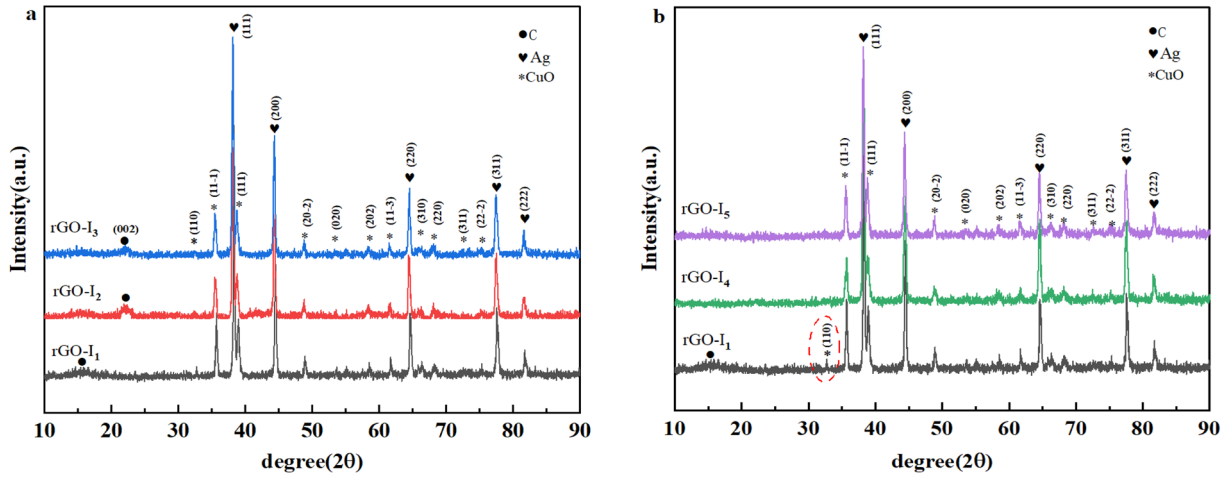

Fig. 1 XRD pattern of Ag@CuO@rGO nanocomposites. (a) Different molar ratios (Cu : Ag = 1 : 1, 1 : 2, 1 : 3, respectively correspond to rGO-I_1, rGO-I_2, rGO-I_3) and (b) varying temperatures and without surfactant.

the particles exhibit different degrees of agglomeration, and decrease in the electron transport capacity.[22]

In particular, without the addition of surfactant (CTAB), the rGO-I_4 showed a small amount of agglomeration using the molar ratio of Cu : Ag = 1 : 1, which causes the Ag@CuO to break away from the rGO, as well as a change in the structure from partially lumpy to capsule-like, Fig. 2j–l, since the addition of surfactant CTAB plays an overwhelmingly important role in regulating the microstructure and surface morphology of Ag@CuO@rGO.[23] Conversely, the addition of CTAB in the right amount will enhance the dispersion of individual component, and promote the close bonding of Ag@CuO and rGO. If the concentration of the added CTAB is too large, the number of micelles in the solution will increase dramatically, and then the agglomeration of the material with CTAB will occur.[24] Fig. 2m–o shows that the Ag@CuO@rGO are more stable in the icing sugar bulk structure with the increase in calcination temperature, but the agglomeration is more serious. Then, the results further demonstrated that the agglomeration decreased the ability of the surface chemistry and reduced the specific capacity.[25,26]

Fig. 2p shows the FETEM of Ag@CuO@rGO; its average diameter was about 103 nm consistent with TEM, and the linear scan of part of Ag@CuO@rGO swept along the direction of the yellow arrow in the red box area. In the meantime, Cu and Ag elements appeared sequentially, and there was the highest intensity of Cu elements at the center of the particle, so as to encapsulate the Ag nanoparticles to form the core–shell structure. Additionally, the C elements were mainly distributed in the core–shell structure Ag@CuO overall particles at various places, which further proved that the Ag@CuO@rGO is a novel core–shell icing block structure. In summary, the hydrothermal synthesis reaction mechanism is shown in Fig. 3. It was demonstrated that the unique structure can significantly improve the electrochemical performance of supercapacitors as an electrode material.[27,28] Thus, the sample rGO-I_1 is the best choice for the subsequent experiment, and the XRD detection also verified the result.

As displayed in (Fig. 4a), the nitrogen adsorption/desorption isotherm of Ag@CuO@rGO was collected. When the relative pressure was in the range of 0–0.5, the adsorption isotherms coincided with the desorption isotherms, which indicated the presence of micropores in Ag@CuO@rGO according to the IUPAC classification.[29] Moreover, in the pressure range is 0.5–0.8, there was a significant hysteresis back loop, this represented the existence of mesopores in Ag@CuO@rGO. Furthermore, when the relative pressure was up to 0.8–1.0, the tailing up can be seen, which is due to the formation of larger pores by particle accumulation. Finally, the specific surface area of Ag@CuO@rGO was approximately 236 $m^2\ g^{-1}$ using the BET method, and the average pore size was tested to be 4 nm, Fig. 4b. That is, the electrolyte can penetrate it better during the charging process of the supercapacitor, resulting in the increase of the reactive sites and the increase of the specific capacitance.

3.2 Electrochemical characterization of Ag@CuO@rGO

3.2.1 Cyclic voltammetry. Fig. 5a illustrates the cyclic voltammetric curves of the prepared Ag@CuO@rGO compounds for the five samples tested in an alkaline electrolyte of 1 mol L^{-1} KOH. The scan rate was set to 20 mV s^{-1}, and the potential window was set to 0.1–0.5 V. The redox peaks of these five curves were symmetrical, which suggested that electron transfer has powerful reversibility. Meanwhile, a pair of obvious reduction-oxidation peaks can be observed around 0.25 V and 0.35 V. According to the reaction mechanism, (1) OH^- ions in the electrolyte will move to the electrode surface under the action of the electric field, and then be adsorbed by the active material on the electrode surface; (2) OH^- ions adsorbed and Ag@CuO will undergo redox reaction on the electrode surface.

The CV curve showed that the reaction was highly reversible, accordingly Cu^{2+} and Cu^+ will interconvert, the reactions are as follows.[30]

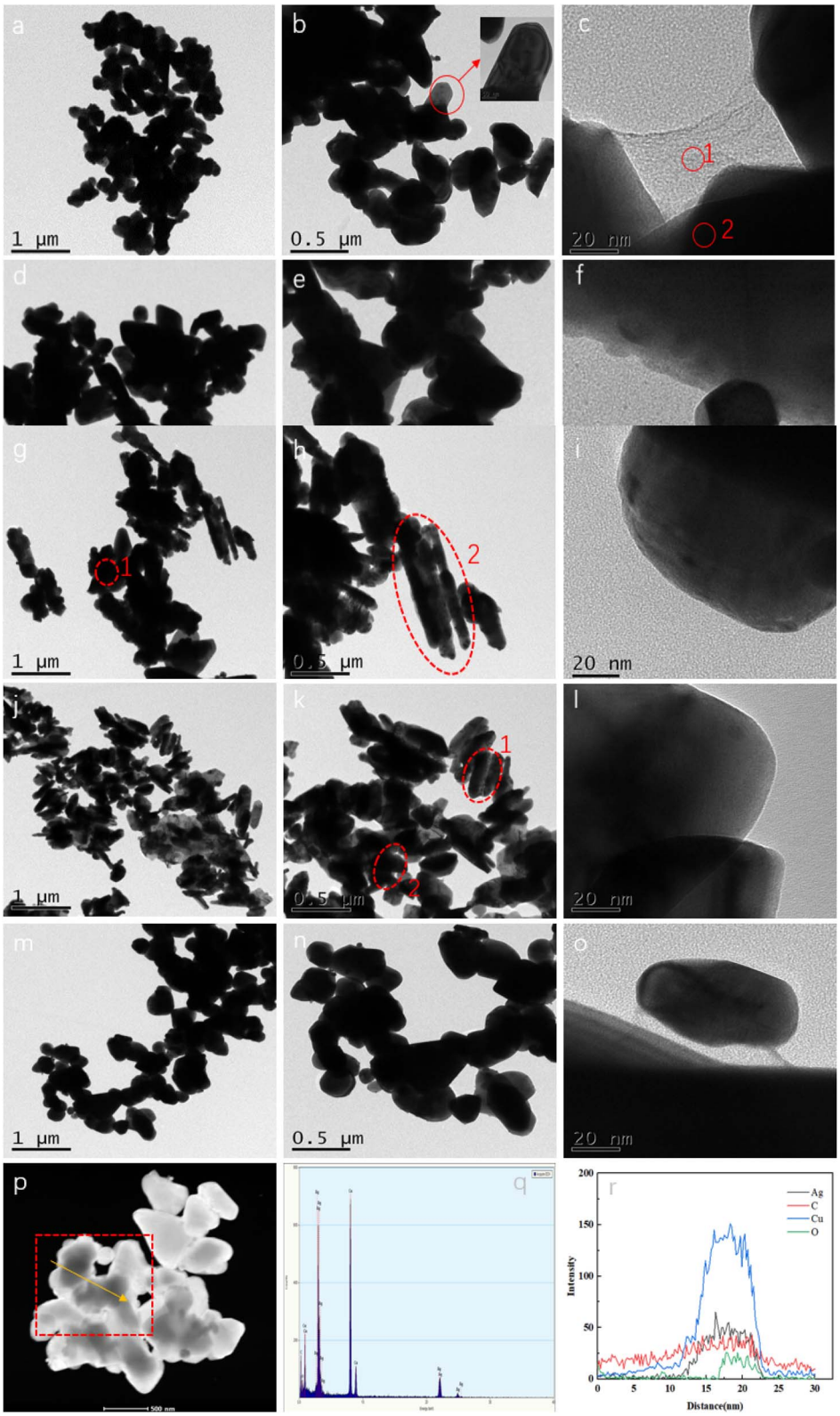

Fig. 2 TEM images of Ag@CuO@rGO nanoparticles with different molar ratio ((a)–(c): rGO-I_1. (d)–(f): rGO-I_2. (g)–(i): rGO-I_3. (j)–(l): rGO-I_4. (m)–(o): rGO-I_5) and FETEM plots ((p)–(r): rGO-I_1).

$$1/2Cu_2O + OH^- \leftrightarrow CuO + 1/2H_2O + e^- \quad (1)$$

$$1/2Cu_2O + 1/2H_2O + OH^- \leftrightarrow Cu(OH)_2 + e^- \quad (2)$$

$$CuOH + OH^- \leftrightarrow CuO + H_2O + e^- \quad (3)$$

$$CuOH + OH^- \leftrightarrow Cu(OH)_2 + e^- \quad (4)$$

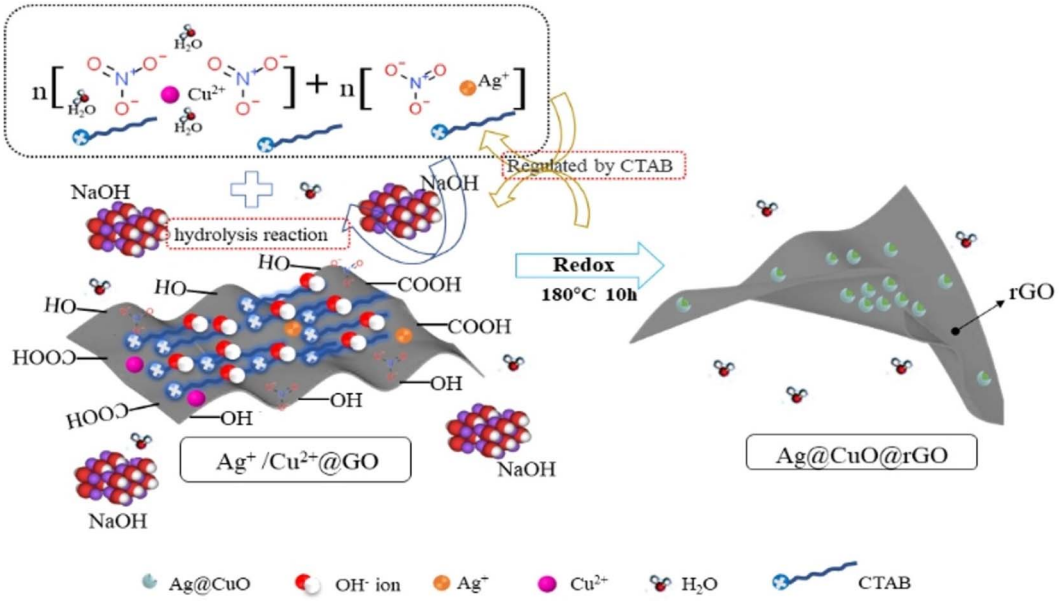

Fig. 3 Formation mechanism of Ag@CuO@rGO.

The molar amount of the added Ag can cause the increase or decrease of the redox peaks in the overall alkaline medium, it is accompanied by a redox reaction of Ag on the Ag@CuO electrode.[31] Because of alkaline electrolytes, the reaction mechanism is postulated as follows: Ag loses electrons and is oxidized to Ag_2O and while being oxidized, the product Ag^+ will further combine with Cu^+ ions to react following eqn (5) and (6):

$$2Ag - 2e^- + 2OH^- \rightarrow Ag_2O + H_2O \quad (5)$$

$$2Ag^+ + 2Cu^+ + 1/2O_2 \leftrightarrow 2Ag^+(Cu^+) + 2Cu^{2+} + O^{2-} \quad (6)$$

As the molar ratio of Cu and Ag increases, there is a tendency for the oxidation peak curve to shift negatively and the reduction peak to shift positively Fig. 5. Consequently, the peak difference is further increased, indicating that a Faraday reaction with a high degree of reversibility occurs at the Ag@CuO electrode,[32] and the doped nano Ag enhanced the reversibility of the electrode reaction. At the same scan rate, the positions of the redox peaks and the shapes of the CV cycling curves of the five samples are the same, and the areas enclosed by them can approximately represent the capacitance size.[28] Since the area size of the cyclic voltammetric are in the order rGO-I_1 > rGO-I_2 > rGO-I_4 > rGO-I_5 > rGO-I_3 the specific capacitance of rGO-I_1 is the largest. Besides, the pseudocapacitance formed by Ag@CuO, a mixed-valence complex that has two redox pairs (Ag^0/Ag^+ and Cu^+/Cu^{2+}).

In consideration of the high conductivity of Ag and rGO, the dispersion property of CTAB, and the high load-bearing property of rGO, CuO doped with Ag and CTAB can enhance its conductivity, and also effectively inhibit the aggregation of nanoparticles and graphene. Therefore, the combination of Ag@CuO and rGO provides better electrochemical performance.[33] However, when the hydrothermal reaction is followed by the higher temperature calcination, it will make the grains

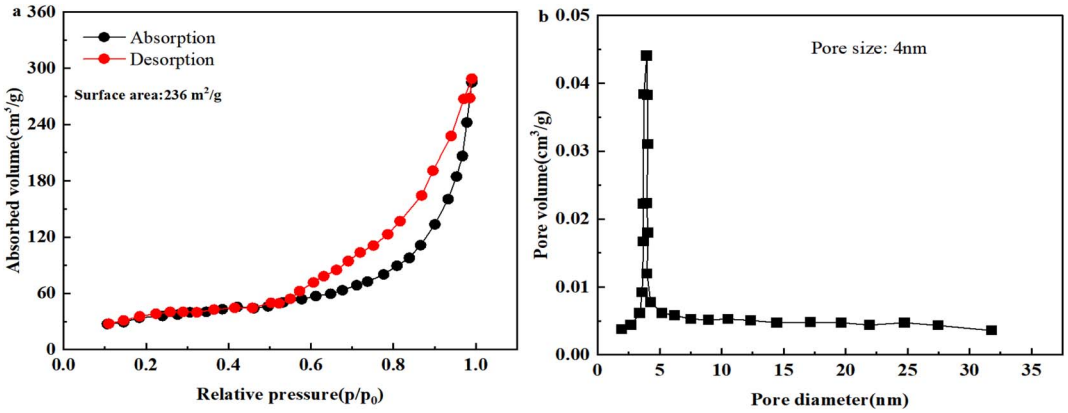

Fig. 4 (a) Adsorption–desorption patterns and (b) pore size distribution of Ag@CuO@rGO of sample rGO-I_1.

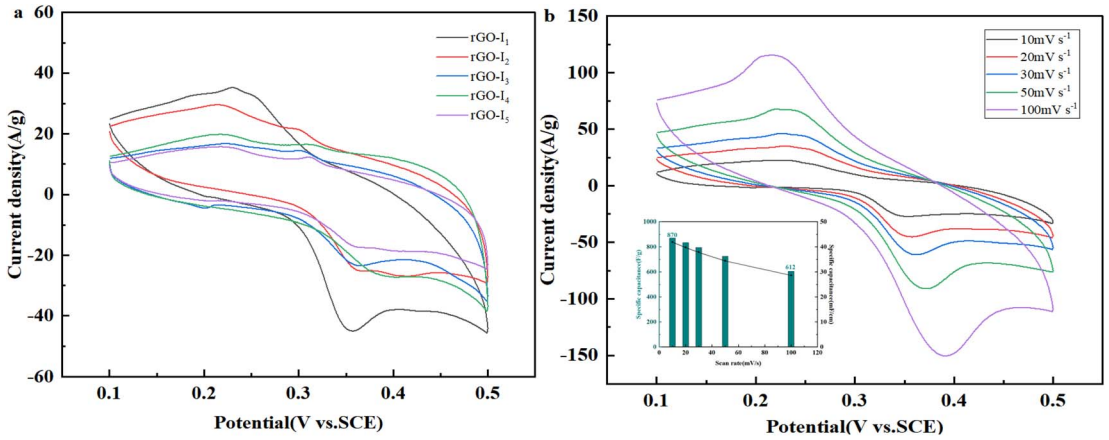

Fig. 5 (a) CVs of rGO-I_i ($i = 1$–5) complex in a 1 mol L^{-1} KOH electrolyte with a scanning rate of 20 mV s^{-1}; (b) CV of sample rGO-I_1 at different sweep speeds, the inset is the specific capacitance of rGO-I_1 and the relationship between capacitance retention at different scan rates.

larger and they will accumulate on the inside and outside of rGO, so as to block the mesh of rGO and reduce the specific surface area, thus leading to a less specific electric capacity of the material.

Fig. 5b displays the CV curves of Ag@CuO@rGO at different sweep rates, that reflect favorable capacitive properties of samples rGO-I_1. With the increase of the scan rate, the oxidation peak and reduction peak tend to move in the positive or negative directions, respectively, and the potential difference increases between the anode and cathode. In addition, the CV curves at different scan rates are completely uniform, this may be on account of enhanced electron polarization at high scan rates, the increased degree of irreversibility,[34] and the issues of mass transfer and charge transfer within the composite.[35]

When electrode compounds are prepared with the addition of surfactant (CTAB) in the molar ratio Cu : Ag = 1 : 1, they have better Faraday pseudocapacitance characteristics. The illustration shows the CV curves calculated from the sample rGO-I_1 and represents the relationship of the specific capacitance, capacitance retention, and different scan rates. The specific capacitance reaches 870 F g^{-1} at a scan rate of 10 mV s^{-1}. Afterward, the scan rate is increased 10 times, the specific capacitance is 612 F g^{-1} and the capacity still reaches more than 70% of the maximum value, which indicates that the Ag@CuO@rGO electrode also has excellent capacitive stability with the increase of scan rate.

3.2.2 Constant-current charge/discharge. Constant current charge/discharge curves of the samples rGO-I_1, rGO-I_2, rGO-I_3, rGO-I_4, and rGO-I_5 are shown in (Fig. 6a–e) at different current densities. It is obvious that the charging and discharging times are relatively symmetric, and the prepared composites have promising reversibility and Coulomb efficiency. In particular, observing the curves of these five groups of samples, all have the longest charging and discharging time at a current density of 2.5 mA cm^{-2}, so the specific capacitance is the largest at this moment, and the specific capacitance values were 1453, 1362, 1208, 1184, and 1082 F g^{-1}, respectively.

Again, the specific capacitance decreased with the amount of Ag gradually increased as a consequence of mass incorporation of Ag@CuO particles formed when excess silver nitrate was added. In this regard, the tremendous increase of agglomerated composite particles is concentrated in the pores of rGO, resulting in a decrease in the specific surface area and a low specific capacitance. As to preparing the samples of rGO-I_4, its specific capacitance is higher than rGO-I_5, which is because the high calcination temperature produces a large particle size resulting in the accumulation of a large number of particles together.

Fig. 6f shows the plots of the multiplicity curves when the current density is reduced from 40–2.5 mA cm^{-2}, the specific capacity preservation remains directly more than 70%, which indicates that Ag@CuO@rGO still has superior multiplicative performance as the current density increases. Moreover, the specific capacitance still has excellent storage capacitance performance using low-current discharge, and it can still meet the current conditions possessed by the electrodes of supercapacitors.

3.2.3 Cyclic specific capacitance. Fig. 7a demonstrates the cyclic specific capacity of rGO-I_i ($i = 1$–5) at a current density of 30 mA cm^{-2}. After 2000 cycles of charging and discharging, the specific capacitance of the samples rGO-I_1 reaches a maximum capacity of 870 F g^{-1}, and the specific capacitance only begins to decrease slowly at the 2200th cycle. When the cycle reached 3000 turns, the specific capacitance was 760 F g^{-1}, which still had 87.36% capacity retention compared to the maximum capacity, showing excellent cycling stability. Additionally, the specific capacities of samples rGO-I_2 and rGO-I_1 are similar, and their rising trend is in agreement. However, the specific capacity values are slightly lower, and the samples rGO-I_3, rGO-I_4, and rGO-I_5 produce extremely severe clumping, resulting in a long rise in specific capacitance owing to the inability of the electrolyte to enter the molecules quickly.

Fig. 7b shows the cycle stability of the samples and rGO-I_1 cannot enter the branch quickly, and the inset is the charge–discharge cycle graph. With the increase of the charge/discharge cycles, there is no capacitance attenuation, and the Coulomb efficiency was close to 100%. The results suggest that the cycling stability of Ag@CuO@rGO obtained from the sample rGO-I_1 has certain cycle stability, and will be used as a high-performance pseudocapacitor material.

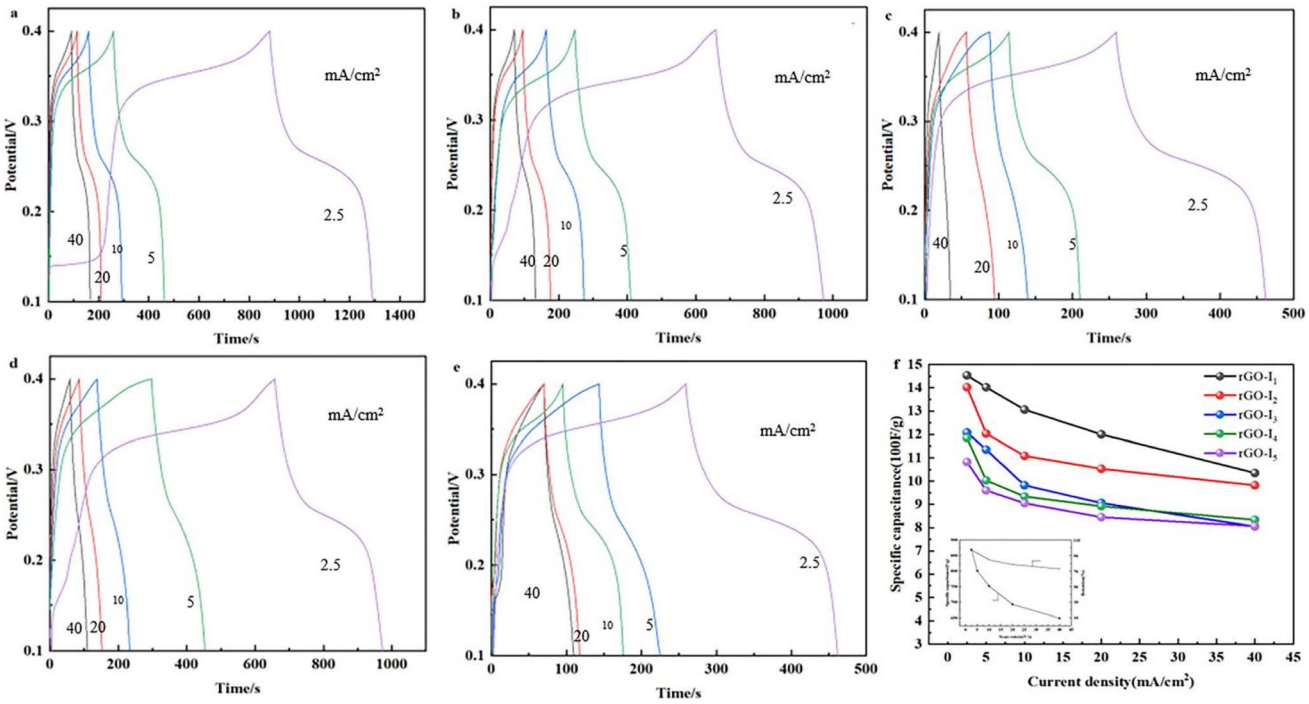

Fig. 6 Constant current charge/discharge curve ((a) rGO-I_1, (b) rGO-I_2, (c) rGO-I_3, (d) rGO-I_4, (e) rGO-I_5) and (f) rGO-I_i ($i = 1$–5) composite rate plots, the inset is the relationship of the specific capacitance (●) and capacitance retention ratio (○) and current density of the sample rGO-I_1.

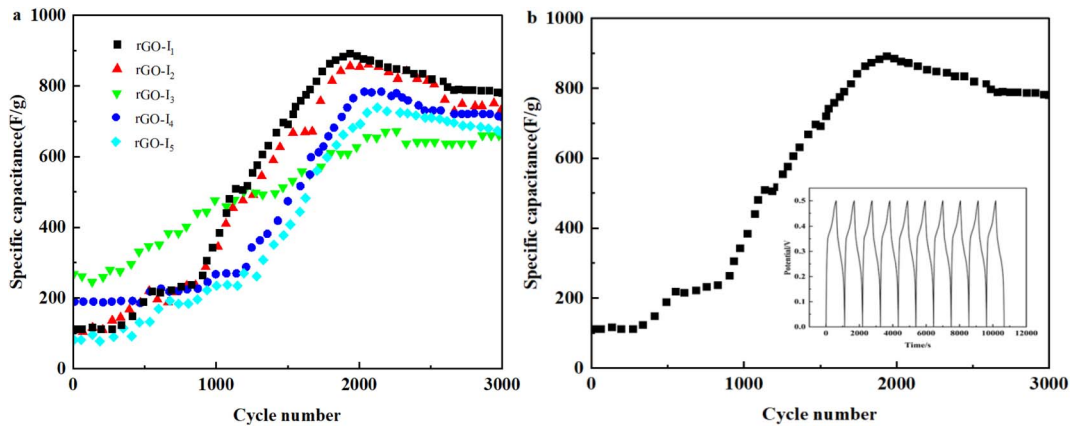

Fig. 7 (a) Cycle curve of each sample at current density of 30 mA cm^{-2}, (b) cycle life diagram of the sample rGO-I_1.

3.2.4 AC impedance characteristics. After comparing the electrochemical properties of the sample rGO-I_i (i = 1–5), the impedance comparison was performed for each sample, as shown in Fig. 8, the open-circuit voltage was set at 0.12 V and the frequency range was 10^{-2} to 10^5 Hz. In the light of the impedance diagram of the equivalent circuit diagram, the Ag@CuO@rGO electrode as the working electrode is shown in the inset. Where R_Ω is the resistance to the solution, Cd_1 and Cd_2 represent the impedance as a result of the ions migration process in the electrode. R_{ct} includes the pseudocapacitive charge transfer resistance and the diffusion resistance in the low-frequency region occurring at the electrode.

The impedance profile curve has an approximate semi-circular shape in the high-frequency region and a straight line in the low-frequency region. Comparing the five curves, the resistance of charge transfer on the Ag@CuO@rGO product has a tendency to get bigger. As the mole ratio of Cu and Ag increased gradually, all of them can still exhibit excellent electrochemical reaction kinetic performance. The low-frequency region represents the diffusion impedance of OH^- ions in the electrolyte around the electrode material, where the magnitude of the slope represents the degree of capacitive properties of the electrode modification material.[36]

Comparing the other three groups of samples, the slope of rGO-I_1 and rGO-I_2 in the low-frequency region is closer to 1.0, indicating a stronger capacitive property.[32] The diameter in the high-frequency region of rGO-I_1 is smaller than that of rGO-I_2, indicating that rGO-I_1 has a smaller charge transfer resistance. In

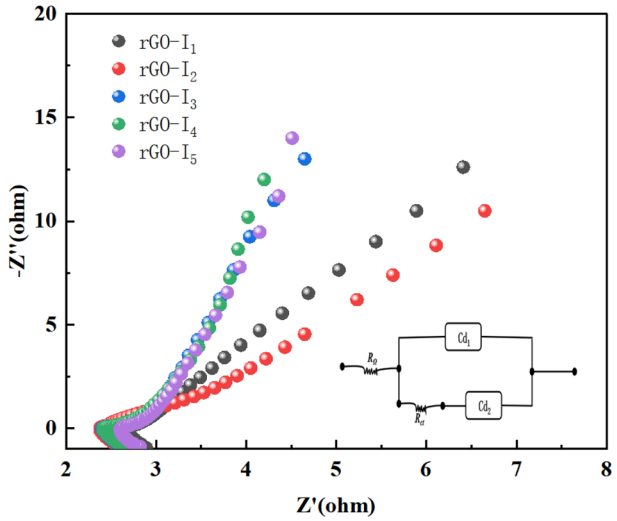

Fig. 8 AC impedance diagram of the sample rGO-I_i ($i = 1$–5), and the inset is equivalent circuit of electrode.

contrast, rGO-I_1 was significantly better than the sample without surfactant rGO-I_4, because the micelles formed by the added surfactant CTAB molecules provided a growth template for the electrode material, and could further promote the close contact between rGO and Ag@CuO, thus its performance in terms of diffusion impedance of electrolyte ions is better than that rGO-I_4.

Furthermore, the impedance performances of GO-I_1 and rGO-I_2 were significantly better than that of rGO-I_5, and the kinetic response of the electrochemical reaction shows the phenomenon of decreasing with the rise in temperature. In conclusion, the sample rGO-I_1 prepared by the ratios have more reliable capacitive performance than the electrode materials.

4 Conclusion

In this study, Ag@CuO nanocomposites consisting of rGO wrapped in icing sugar nucleophile structure were synthesized successfully using various methods, and morphology analysis and subsequent electrochemical characterization tests were performed. Furthermore, we analyzed the influence between the electrochemical properties and different morphologies.

The composites prepared with a molar ratio of Cu : Ag = 1 : 1 have good dispersion and homogeneity and exhibit excellent electrochemical performance as electrode modification materials in supercapacitors. Compared to the other composites, the results indicate that it has a high specific capacitance of 1453 F g^{-1} at a current density of 2.5 mA cm^{-2}, and the charge–discharge cycle test of the material showed that the sample rGO-I_1. Importantly, it is proved that the Ag@CuO@rGO nano-composite could be applied to supercapacitors on account of charge/discharge efficiency and multiplicity performance.

Conflicts of interest

There are no conflicts to declare.

References

1 Z. S. Iro, C. Subramani and S. S. Dash, A brief review on electrode materials for supercapacitor, *Int. J. Electrochem. Sci.*, 2016, **11**(12), 10628–10643.
2 A. Burke, Ultracapacitors: why, how, and where is the technology, *J. Power Sources*, 2000, **91**(1), 37–50.
3 R. Liang, Y. Du, P. Xiao, J. Cheng, S. Yuan, Y. Chen and J. Chen, Transition metal oxide electrode materials for supercapacitors: a review of recent developments, *Nanomaterials*, 2021, **11**(5), 1248.
4 S. Jin, H. Lee and S. Yim, Enhanced capacitive properties of all-metal-oxide-nanoparticle-based asymmetric supercapacitors, *RSC Adv.*, 2019, **9**(55), 31846–31852.
5 R. R. Bi, X. L. Wu, F. F. Cao, L. Y. Jiang, Y. G. Guo and L. J. Wan, Highly dispersed RuO_2 nanoparticles on carbon nanotubes: facile synthesis and enhanced supercapacitance performance, *J. Phys. Chem. C*, 2010, **114**(6), 2448–2451.
6 C. Kong, W. Lu, J. Zong, F. Pu, X. Hu, X. Zhang and H. Jin, Template-assisted synthesis of CuO hollow nanotubes constructed by ultrathin nanosheets for lithium-ion battery applications, *J. Alloys Compd.*, 2020, **849**, 156635.
7 C. Batchelor-McAuley, Y. Du, G. G. Wildgoose and R. G. Compton, The use of copper (II) oxide nanorod bundles for the non-enzymatic voltammetric sensing of carbohydrates and hydrogen peroxide, *Sens. Actuators, B*, 2008, **135**(1), 230–235.
8 E. Reitz, W. Jia, M. Gentile, Y. Wang and Y. Lei, CuO nanospheres based nonenzymatic glucose sensor, *Electroanalysis*, 2008, **20**(22), 2482–2486.
9 M. R. Mahmoudian, W. J. Basirun and Y. Alias, Synthesis of 3D hierarchical Ag/CuO nano-structures in the presence of l-histidine and their application, *J. Alloys Compd.*, 2017, **699**, 803–811.
10 L. H. Mendoza-Huizar, M. Palomar-Pardave and J. Robles, A theoretical quantum study on the distribution of electrophilic and nucleophilic active sites on the Au (100) surface modeled as finite clusters, *J. Mol. Struct.: THEOCHEM*, 2004, **679**(3), 187–194.
11 Y. Li, P. C. Yin, Y. X. Zhang and R. Z. Zhang, Synthesis of honeycomb Ag@CuO nanoparticles and its application as a highly sensitive and electrocatalytically active hydrogen peroxide sensor material, *Anal. Methods*, 2022, **14**, 4842–4850.
12 D. D. Zhi, T. Li, J. Z. Li, H. S. Ren and F. B. Meng, A review of three-dimensional graphene-based aerogels: synthesis, structure and application for microwave absorption, *Composites, Part B*, 2021, **211**, 108642.
13 W. Wang, J. Meng, Y. Hu, J. Wang, Q. Li and J. Yang, Thgraphene: a novel two-dimensional carbon allotrope as a potential multifunctional material for electrochemical water splitting and potassium-ion batteries, *J. Mater. Chem. A*, 2022, **10**(18), 9848–9857.
14 Y. Liu, Y. Ying, Y. Mao, L. Gu, Y. Wang and X. Peng, CuO nanosheets/rGO hybrid lamellar films with enhanced capacitance, *Nanoscale*, 2013, **5**(19), 9134–9140.

15 B. Wang, X. L. Wu, C. Y. Shu, Y. G. Guo and C. R. Wang, Synthesis of CuO/graphene nanocomposite as a high-performance anode material for lithium-ion batteries, *J. Mater. Chem.*, 2010, **20**(47), 10661–10664.

16 D. A. Kospa, A. I. Ahmed, S. E. Samra and A. A. Ibrahim, High efficiency solar desalination and dye retention of plasmonic/reduced graphene oxide based copper oxide nanocomposites, *RSC Adv.*, 2021, **11**(25), 15184–15194.

17 P. Viswanathan, K. Wang, J. Li and J. D. Hong, Multicore–shell Ag–CuO networked with CuO nanorods for enhanced non-enzymatic glucose detection, *Colloids Surf., A*, 2020, **598**, 124816.

18 D. J. Joshi, J. R. Koduru, N. I. Malek and C. M. Hussain, Surface modifications and analytical applications of graphene oxide: a review, *TrAC, Trends Anal. Chem.*, 2021, **144**, 116448.

19 H. M. Hassan, V. Abdelsayed, S. K. Abd El Rahman, K. M. AbouZeid, J. Terner, M. S. El-Shall and A. A. El-Azhary, Microwave synthesis of graphene sheets supporting metal nanocrystals in aqueous and organic media, *J. Mater. Chem.*, 2009, **19**(23), 3832–3837.

20 C. Nethravathi, T. Nisha, N. Ravishankar, C. Shivakumara and M. Rajamathi, Graphene-nanocrystalline metal sulphide composites produced by a one-pot reaction starting from graphite oxide, *Carbon*, 2009, **47**(8), 2054–2059.

21 Y. Li, C. N. Duan, Z. Jiang, X. B Zhou and Y. Wang, CuO/rGO nanocomposite as an anode material for high-performance lithium-ion batteries, *Mater. Res. Express*, 2021, **8**(5), 055505.

22 M. D. Adams, The mechanism of adsorption of aurocyanide onto activated carbon, 1. Relation between the effects of oxygen and ionic strength, *Hydrometallurgy*, 2010, **29**(6), 997–1003.

23 N. Begletsova, E. Selifonova, A. Chumakov, A. Al-Alwani, A. Zakharevich, R. Chernova and E. Glukhovskoy, Chemical synthesis of copper nanoparticles in aqueous solutions in the presence of anionic surfactant sodium dodecyl sulfate, *Colloids Surf., A*, 2018, **552**, 75–80.

24 E. Kurowska, A. Brzózka, M. Jarosz, G. D. Sulka and M. Jaskuła, Silver nanowire array sensor for sensitive and rapid detection of H_2O_2, *Electrochim. Acta*, 2013, **104**, 439–447.

25 A. A. Khaleed, A. Bello, J. K. Dangbegnonc, M. J. Madito, O. Olaniyan, F. Barzegar and N. Manyala, Solvothermal synthesis of surfactant free spherical nickel hydroxide/graphene oxide composite for supercapacitor application, *J. Alloys Compd.*, 2017, **721**, 80–91.

26 D. D. Zhao, S. J. Bao, W. J. Zhou and H. L. Lic, Preparation of hexagonal nanoporous nickel hydroxide film and its application for electrochemical capacitor, *Electrochem. Commun.*, 2007, **9**(5), 869–874.

27 X. Zhang, J. Ma, W. Yang, Z. Gao, J. Wang, Q. Liu, J. Liu, J. Y. Liu and X. Y. Jing, Manganese dioxide core–shell nanowires in situ grown on carbon spheres for supercapacitor application, *CrystEngComm*, 2014, **16**(19), 4016–4022.

28 Y. Qiu, J. Yu, G. Fang, H. Shi, X. Zhou and X. Bai, Synthesis of carbon/carbon core/shell nanotubes with a high specific surface area, *J. Phys. Chem. C*, 2009, **113**(1), 61–68.

29 J. Rouquerol and F. Rouquerol, *Adsorption by powders and porous solids: principles, methodology and applications*, Academic Press, US, 2013.

30 C. Zhu, S. Guo, Y. Zhai and S. Dong, Layer-by-layer self-assembly for constructing a graphene/platinum nanoparticle three-dimensional hybrid nanostructure using ionic liquid as a linker, *Langmuir*, 2010, **26**(10), 7614–7618.

31 K. Kuratani, T. Kiyobayashi and N. Kuriyama, Influence of the mesoporous structure on capacitance of the RuO_2 electrode, *J. Power Sources*, 2009, **189**(2), 1284–1291.

32 C. Barbero, G. A. Planes and M. C. Miras, A novel microarray chemiluminescence method based on chromium oxide nanoparticles catalysis for indirect determination of the explosive triacetone triperoxide at the scene, *Electrochem. Commun.*, 2001, **3**(3), 113–116.

33 Y. Zhang, X. P. Xiao, Y. J. Sun, Y. Shi, H. C. Dai, P. J. Ni, J. T. Hu, Z. Li, Y. H. Song and L. Wang, Electrochemical deposition of nickel nano-particles on reduced graphene oxide film for nonenzymatic glucose sensing, *Electroanalysis*, 2013, **25**(4), 959–966.

34 S. B. Yang, X. L. Wu, C. L. Chen, H. L. Dong, W. P. Hu and X. K. Wang, Spherical a-$Ni(OH)_2$ nanoarchitecture grown on graphene as advanced electrochemical pseudocapacitor materials, *Chem. Commun.*, 2012, **48**, 2773–2775.

35 M. Aghazadeh, M. Hosseinifard, B. Sabour and S. Dalvand, Pulse electrochemical synthesis of capsule-like nanostructures of Co_3O_4 and investigation of their capacitive performance, *Appl. Surf. Sci.*, 2013, **287**, 187–194.

36 H. Xu, J. Zhuang, Y. Chen, J. Wu and J. Zhang, Preparation and performance of Co_3O_4-NiO composite electrode material for supercapacitors, *RSC Adv.*, 2014, **4**(30), 15511–15517.